Constructing a stable cobalt-nitrogen-carbon air cathode from coordinatively unsaturated zeolitic-imidazole frameworks for rechargeable zinc-air batteries

Tingting Wang, Meng Liu, Somboon Chaemchuen, Jichao Wang, Ye Yuan, Cheng Chen, Ang Qiao (✉), Francis Verpoort (✉), and Zongkui Kou (✉)

State Key Laboratory of Advanced Technology for Materials Synthesis and Processing, Wuhan University of Technology, Wuhan 430070, China

ABSTRACT

Zeolitic-imidazole frameworks (ZIFs) derivations have widely emerged as an efficient air cathode of zinc-air batteries (ZABs) due to excellent bifunctional oxygen electrocatalysis performance. However, they are not stable enough for long-term operation of rechargeable ZABs because of weak association with current collector, especially under bending conditions for flexible ZAB devices. Here, we show that by purposely designing coordinatively unsaturated ZIFs via a facile morphology regulation, which can be chemically linked on acid-treated carbon cloth, a stable Co-N-C air cathode is therefore derived where Co nanoparticles (NPs) are uniformly confined within the Co-N-C matrix on carbon cloth (Co/Co-N-C/CC). Specifically, when without being stabilized from carbon cloth, the pyrolysis of ZIFs with different unsaturated coordination levels has a negligible impact on the bifunctional oxygen-catalyzed performance. The optimal Co/Co-N-C/CC catalyst assembled ZAB possesses a large open circuit voltage of 1.415 V and a high peak power density of 163 mW·cm⁻² as well as excellent cycling durability upon 630 discharge–charge cycles with 61% voltage efficiency remained, largely exceeding those of a benchmark Pt/C-IrO₂ catalyst assembled ZAB. The synergy between Co NPs and active Co-N-C sites via electronic interaction induces the outstanding bifunctional oxygen-catalyzed activity and cathode performance. The present work highlights the importance of unsaturated coordination structures in ZIFs precursors for the performance of derived nanostructures in integrated electrodes.

KEYWORDS

coordinatively unsaturated zeolitic-imidazole frameworks (ZIFs), cobalt-nitrogen-carbon, bifunctional air electrodes, zinc-air battery, flexible electrode

1   Introduction

Concern is growing over this new period of zinc-air battery (ZAB) due to the high theoretical energy density (1,084 Wh·kg⁻¹), earth-abundant Zn source, and good security [1, 2]. However, its performance is restricted by insufficient oxygen electrocatalysis kinetics at the cathode side. Currently, the benchmark cathode materials for redox system are noble and scarce Pt, Ir, and Ru-based nanomaterials, but exorbitant cost, poor stability, and single functionality have become the main obstacles for their further development [3–6]. For this purpose, numerous efforts have been dedicated to exploring non-noble, bifunctional, and stable electrocatalysts. Among a plenty of choices, transition metal-nitrogen-carbon (TM-N-C) materials have been demonstrated to be a promising candidate of bifunctional cathode catalyst on basis of high intrinsic activity on TM-N-C centers and tunable local electronic configurations in addition to good conductivity and flexible hierarchical structure control [7–11].

Zeolitic-imidazole frameworks (ZIFs) as a significant branch of metal organic frameworks have been commonly used to derive various TM-N-C materials, in which TM nodes and imidazole ligands afford abundant active TM-N_x-C centers (e.g., Co-, Fe-, and Ni-N_x-C) and/or nitrogen-doped carbon matrix [12, 13]. On account of the inherited structural advantages assisted with processing easiness of ZIF precursors, excellent bifunctionality towards oxygen electrocatalysis has been gained by pyrolyzing ZIFs into the desired nanostructures [14, 15]. Unfortunately, when these derivative powders are employed in the rechargeable ZAB cathodes, the weak immobilization between current-collecting (e.g., carbon cloth and nickel foam) and powder samples leads to poor long-term durability [16, 17]. Recently, extensive progresses have been realized by growing ZIFs on the acid-treated carbon cloth for manufacturing integrated cathode with robust stability in the application of rechargeable ZABs [18, 19]. For example, Guan et al. modified the functional groups (i.e., –COOH, –C=O, and –COH) on the carbon cloth to stabilize active components on the integrated electrodes [20, 21]. In another typical example, Al₂O₃ protection layer has been manifested for stabilizing Zn/Co-ZIF-derivatives on carbon cloth via capturing volatile carbon- and nitrogen-containing species during the thermal decomposition [22]. Nevertheless, the adhesive strength of carbon cloth fiber still has a large space to improve.

Herein, we purposely design various shaped ZIFs with same (Co-imidazole) links yet different level of open coordination sites via a simple coprecipitation method. The electrochemical

Address correspondence to Ang Qiao, qiaoang@whut.edu.cn; Francis Verpoort, Francis@whut.edu.cn; Zongkui Kou, zongkuikou@whut.edu.cn

performance of derivatives from the above-mentioned ZIFs initially demonstrates a similar bifunctional level towards oxygen electrocatalysis. We found that the leaf-like ZIF (denoted as ZIF-L) with highest unsaturated coordination level can be most strongly bonded on the acid-treated carbon cloth substrate to give an integrated electrode. The integrated electrode was therefore fabricated as a free-standing air cathode of flexible rechargeable ZABs, which verifies an ultrahigh open circuit voltage of 1.415 V and a large peak power density of 163 mW·cm^{-2} as well as excellent cycling durability upon 630 discharge–charge cycles with 61% voltage efficiency remained. These results outperform those of benchmarking Pt/C-IrO$_2$ hybrid and most catalysts in the latest reports. We hope this rational study on structure-performance relationship would shine the light on designing robust integrated electrodes for practical energy technologies.

2   Results and discussion

For digging into the effect of the coordination unsaturated sites of ZIF precursors, the evolution process was regulated by solvent-induced growth method [23]. Herein, different volume ratios of solvent H$_2$O to CH$_3$OH were used (for more details see Table S1 in the Electronic Supplementary Material (ESM)) to derive various morphological ZIFs. The microstructure of as-synthesized products was studied by scanning electron microscopy (SEM), as shown in Figs. S1–S3 in the ESM. Analyzing by the powder X-ray diffraction (PXRD) patterns (Fig. S4 in the ESM), rhombic dodecahedron-like ZIF corresponds to ZIF-67 (denoted as ZIF-R), and the leaf-like ZIF coincides with ZIF-L [24, 25]. Another two contrast shapes of ZIF are the flower-like (denoted as ZIF-F). The XRD pattern of ZIF-F demonstrates that it is very close to the phase structure of ZIF-67, which is also manifested by the SEM image in Fig. S2 in the ESM, where the outer surface of the ZIF-F is enclosed by cube crystals. Additionally, the peak intensity of ZIF-L is weaker than those of ZIF-R and ZIF-F, suggesting that the crystallinity of ZIF-L could be poorer than those of another two shapes of ZIFs possibly due to the more unsaturated coordination [26].

The NH$_3$-temperature programmed desorption (TPD) and CO$_2$-TPD analyses are widely used to identify and compare the uncoordinated metal species and ligands in ZIF precursors, respectively [27, 28]. The NH$_3$-TPD integral area of ZIF-L is calculated to be 14.6 and 1.5 times that of ZIF-F and ZIF-R, respectively (Figs. 1(a) and 1(c)). The CO$_2$-TPD results follow the same trend as follows: ZIF-L > ZIF-F > ZIF-R (Figs. 1(b) and 1(d)). In addition, the high temperature desorption peak of ZIF-L shifts to the left obviously. This implies that almost non-porous structure of ZIF-L limits the rapid diffusion of NH$_3$, which makes the desorption temperature relatively low. Clearly, ZIF-L has exhibited the highest structural integrity among all the ZIF precursors upon exposure to both NH$_3$ and CO$_2$, indicating that the ZIF-L has the most content of unsaturated coordination. As illustrated in the schematic diagram of Fig. 1(e), these unsaturated coordination bonds could provide opportunities for bonding with surface-enhanced functional groups of carbon substrates (–COOH, –OH, and –C=O) [29].

To identify the unsaturated coordination level of ZIF precursors on the microstructure and performance of the derived Co-N-C products, their morphology and structure difference are first characterized by SEM and transmission electron microscopy (TEM) measurements. The derivatives are denoted as ZIF-X-D where X represents the shape of ZIF. Figures 2(a)–2(c) demonstrate their morphological characteristics of ZIF precursors inserted with shape models. Clearly, the ZIF-R-D inherits the morphology of ZIF-R but obvious shrinkage with abundant carbon nanotubes (CNTs) on the surfaces (Fig. 2(d)). The derivations from ZIF-F-D and ZIF-L-D reversely presents a morphology evolution (Figs. 2(e) and 2(f)), yet a less amount of CNTs can be seen. TEM images unveil the existence of graphitic carbon layers on the Co nanoparticles (NPs) in all the derivations (Figs. 2(g)–2(i)). In the ZIF-L-D, Co NPs with an average size of about 20 nm are wrapped in carbon nanocages (CNCs). Both ZIF-R-D and ZIF-F-D derive a different microstructure where Co NPs are encapsulated within multi-walled CNTs. XRD patterns of the derivations (Fig. S5 in the ESM) demonstrate that there are a (002) diffraction peak indexing to graphitic carbon and three distinct peaks at 44.3°, 51.6°, and 75.8° indexing to Co phase (JCPDS No. 15-0806), respectively [30, 31]. The Brunauer–Emmett–Teller (BET) analyses of ZIFs furtherly gives a large difference of specific surface area (SSA) among both ZIF precursors and products (Figs. S6–S10 and Table S2 in the ESM). For example, ZIF-R demonstrates the largest surface area of 1,883 m^2·g^{-1} while ZIF-L only possesses an extremely low SSA value of 3.7 m^2·g^{-1}.

Inductively coupled plasma (ICP) and X-ray photoelectron spectra (XPS) characterizations were then conducted to analyze the content of element, elemental compositions, and chemical status in the studied samples. As given in Table S3 in the ESM, the active Co content in the ZIF-X-D follows a decreasing trend (ZIF-
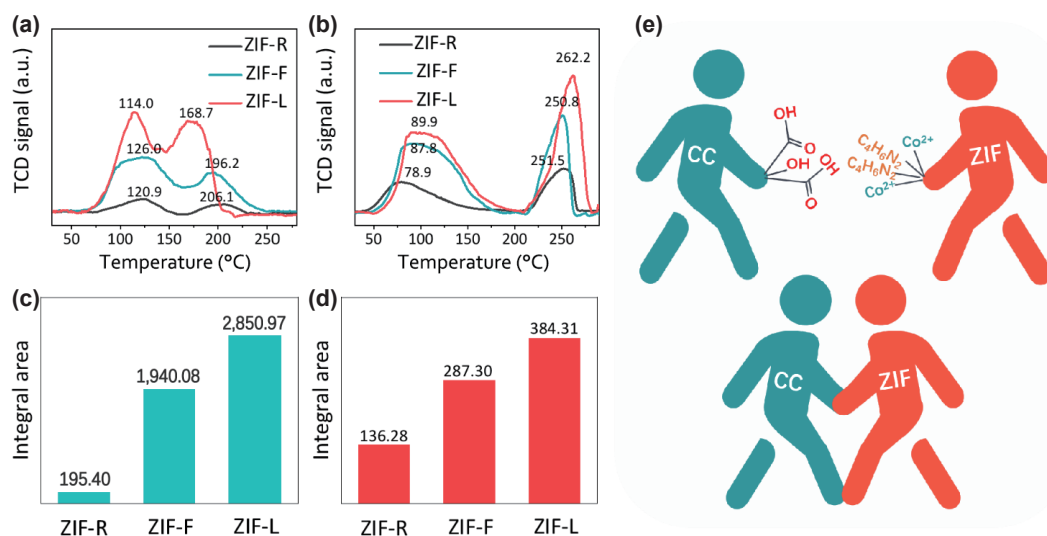

Figure 1   (a) and (b) The NH$_3$-TPD and CO$_2$-TPD profiles of the ZIF-R, ZIF-F, and ZIF-L. (c) and (d) Integral area of desorption peak of the ZIF-R, ZIF-F, and ZIF-L. (e) An illustration of the preparation of ZIFs grown on carbon cloth.
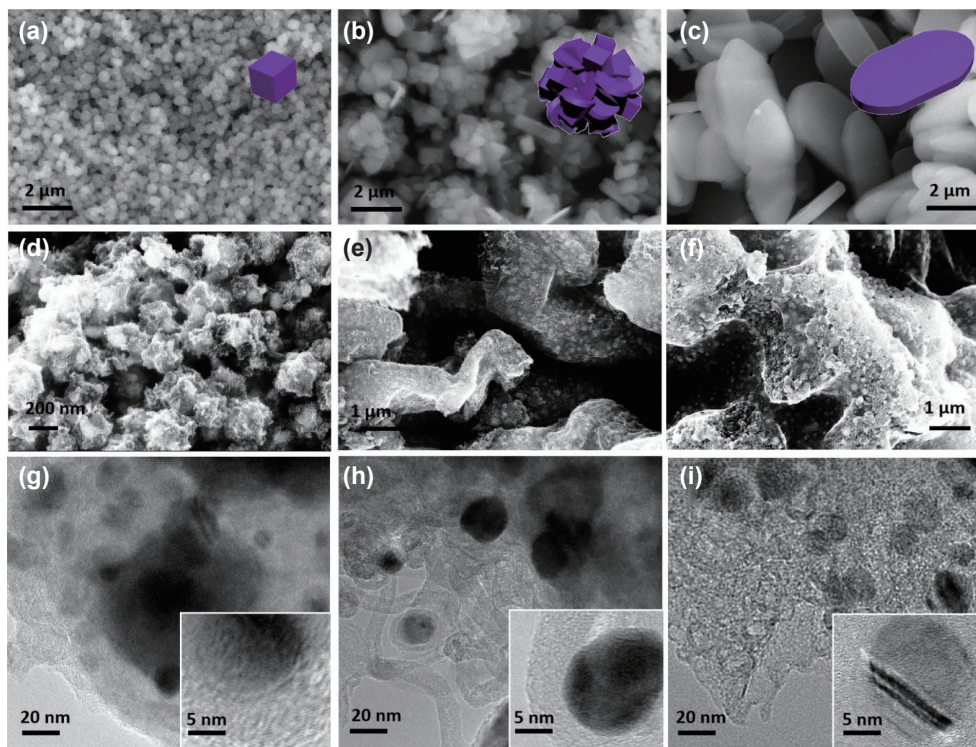
Figure 2 The SEM and TEM images of ZIF-X and ZIF-X-D. (a)–(c) SEM images of ZIF-R, ZIF-F, and ZIF-L, respectively, (d)–(f) SEM images of ZIF-R-D, ZIF-F-D, and ZIF-L-D, respectively, and (g)–(i) TEM images and insets are the corresponding lattice fringes of Co NPs in ZIF-R-D, ZIF-F-D, and ZIF-L-D, respectively.

L-D < ZIF-F-D < ZIF-R-D). The binding states of C, N, O, and Co in ZIF-X-D were identified by XPS spectra (Fig. S11 in the ESM). The high-resolution N 1s spectra displays two prominent peaks, corresponding to Co–N_x (398.8–398.9 eV) and graphitic N (401.0–401.4 eV) (Fig. S12 in the ESM) [32, 33]. The C 1s XPS spectra reveal the coexistence of C–C (284.7–284.8 eV), C=N (285.3–285.7 eV), C–O (286.6–286.9 eV), and C=C (290.3 eV) (Figs. S13(a)–S13(c) in the ESM) [34]. The Co 2p XPS spectra can fit well with two peaks at 779.9 and 795.7 eV, which are assigned to Co $2p_{3/2}$ and Co $2p_{1/2}$, respectively [32]. We therefore conclude

that all of them present quite different microstructures, elemental contents, and chemical states which could therefore produce a key influence on the oxygen electrocatalysis.

Next, the bifunctional oxygen reduction reaction/oxygen evolution reaction (ORR/OER) activities of as-prepared ZIF-X-D were estimated in O_2-saturated 0.1 M KOH electrolyte with a rotating disk configuration (RDE, 1,600 rpm). The linear sweep voltammetry (LSV) curves in Fig. 3(a) reveal a very close half-wave potential ($E_{1/2}$) on the ZIF-R-D (0.83 V vs. reversible hydrogen electrode (RHE)), ZIF-F-D (0.85 V vs. RHE), and
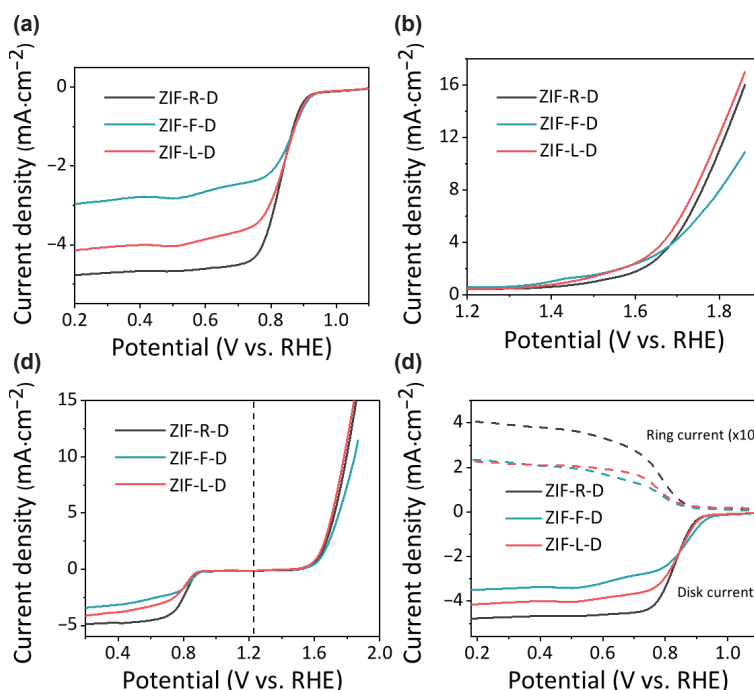

Figure 3 Catalytic performance of the ZIF-X-D for ORR and OER. (a) LSV curves of ZIF-X-D for ORR in O_2-saturated 0.1 M KOH at 1,600 rpm; (b) LSV curves of ZIF-X-D for OER; and (c) LSV curves towards bifunctional ORR/OER. (d) Rotating ring-disk electrodes (RRDE) tests (1,600 rpm) of various electrodes derived from ZIF-X-D for ORR in 0.1 M KOH saturated with oxygen at a scan rate of 5 mV·s^{-1}.

ZIF-L-D (0.84 V vs. RHE), respectively. Moreover, all of ZIF-R-D, ZIF-F-D, and ZIF-L-D also deliver a relatively large potential of 1.79, 1.84, and 1.77 V vs. RHE at the current density of 10 mA·cm^{-2} (Fig. 3(b)), respectively. The bifunctional electrocatalytic activity and reversibility for ORR/OER are evaluated by $\Delta E = E_{j10} - E_{1/2}$. As shown in Fig. 3(c), ZIF-L-D exhibits a slightly lower of ΔE (0.93 V) than those of ZIF-F-D (0.99 V) and ZIF-R-D (0.96 V). The LSV at different rotation rates is collected to calculate the electron transfer numbers (*n*) based on the Koutecky–Levich equation at the potential range of 0.5–0.7 V vs. RHE (Fig. 3(d)) [35]. All of them demonstrate a four-electron ORR pathway (Figs. S14–S16 in the ESM). Among these three samples, ZIF-L-D only presents a slightly better bifunctional catalytic performance probably because it possesses a quite highest SSA and best structural feature, as well as a largest unsaturated coordination level in the precursor.

Inspired by the special unsaturated coordination structure, ZIF-L was therefore *in situ* grown on the carbon cloth surfaces for the evaluation of battery performance. The carbon cloth (CC) was first acidified by concentrated nitric acid (HNO$_3$). The assembly process is schematically present in Fig. 4(a), where functionalized carbon cloth was modified by 2-methylimidazole (2-MIM), and the cobalt nitrate was then introduced. Although ZIF grown on modified carbon cloth fiber shares the same mother liquor with ZIF-L powder, the substrate–precursor coactions notably affect the morphology [36]. Figure 4(b) gives the digital pictures of the preparation process of ZIFs on carbon cloth. Sword-like ZIF arrays grow on carbon cloth (denoted as ZIF-S@CC) along proliferative *Z*-axis direction (Fig. 4(c)). Although the heteropeak of ZIF-S@CC is obvious influenced by the higher background noise from the carbon cloth. The characteristic peak corresponding to ZIF-L can be verified by XRD patterns (Fig. S17 in the ESM) [37]. ZIF-S@CC was then treated under the identical carbonization condition as the powder samples. The broad peaks located between 20° and 30° in the XRD pattern correspond to the carbon cloth. The peaks at 44.3°, 51.6°, and 76.0° can be indexed to the (111), (200), and (220) lattice planes of metallic Co (JCPDS No. 15-0806) [38] (Fig. S18 in the ESM). At some local part, the carbonated derivatives retain the novel sword-like morphology, but vast majority of the ZIFs skeleton collapse (Fig. 4(d)). From the magnified images, approximately 50 nm Co NPs are uniform embedded on carbon cloth (Figs. 4(e) and 4(f)). The carbon cloth
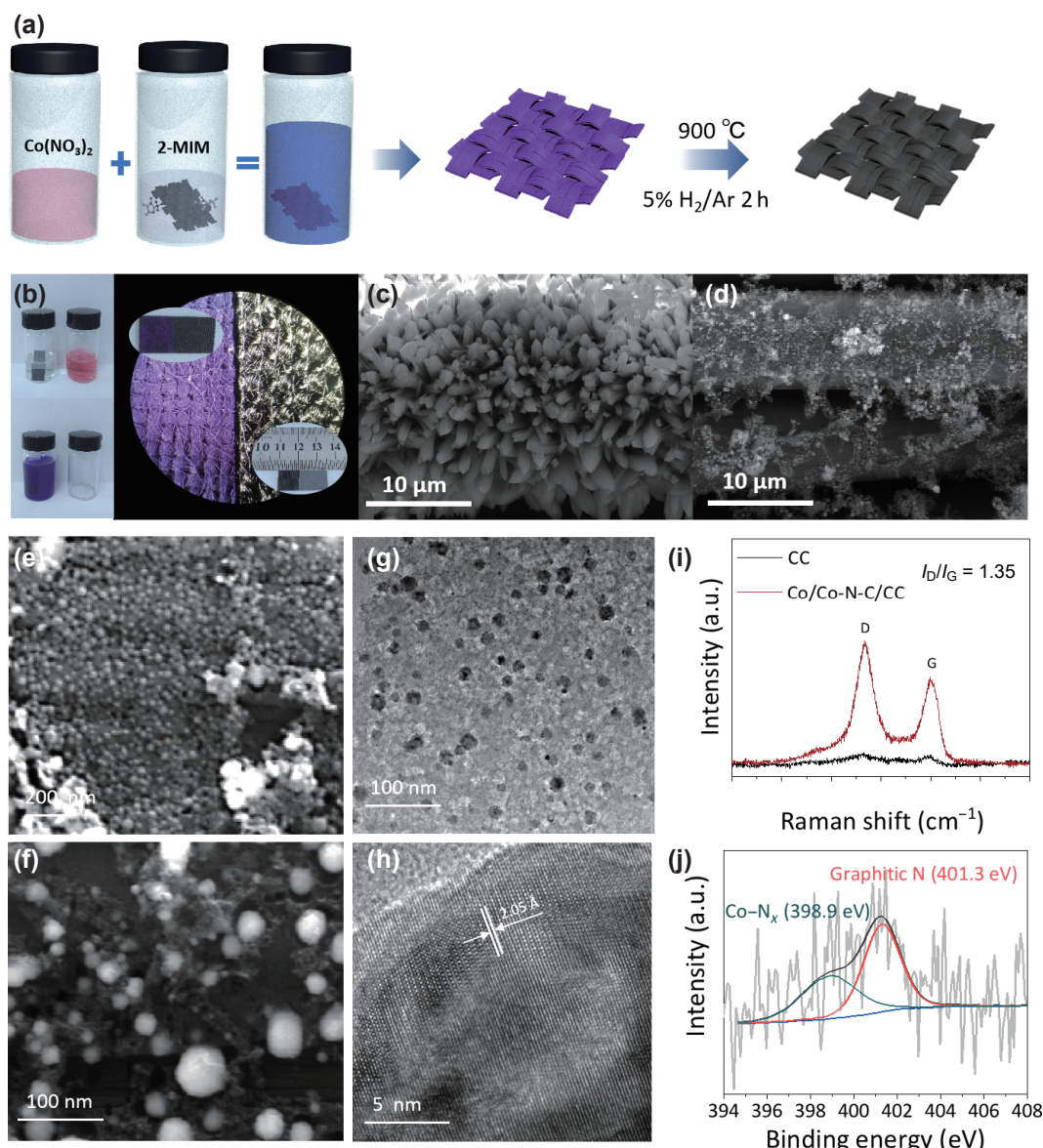

Figure 4 Preparation and electron microscopy characterization of ZIF-S@CC. (a) Schematic illustration toward the synthetic process of ZIF-S@CC. (b) Photographs of 4 mL scale synthesis. SEM images of (c) ZIF-S@CC and (d) Co/Co-N-C/CC. (e) and (f) SEM images of Co NPs anchored on carbon fiber, (g) TEM image of Co NPs wrapped in carbon matrix, (h) high-magnification TEM images of Co NPs, (i) Raman spectra of CC and Co/Co-N-C/CC, and (j) high-resolution N 1s XPS spectra of Co/Co-N-C/CC.

shows evident surface roughness which is probably caused by the corrosion and oxidation in the high concentrated HNO_3 solution. Whereas, the surface of untreated carbon cloth fibers is much smoother (Fig. S19 in the ESM). Co NPs with averagely ~ 20 nm are homogeneous dotted in the local undestroyed carbon matrix (Fig. 4(g)). The existence of Co (JCPDS No. 15-0806) [39] is reconfirmed by high-resolution TEM (HRTEM) image, where the identified lattice fringes (2.05 Å) are consistent with the (111) plane (Fig. 4(h)). All of C, N, O, and Co species can be detected in Co/Co-N-C/CC by full XPS spectrum (Fig. S20 in the ESM). The deconvoluted peaks at 779.2 and 794.7 eV are assigned to the Co $2p_{3/2}$ and $2p_{1/2}$, respectively, in the Co 2p spectrum (Fig. S21 in the ESM) [40]. The high-resolution C 1s spectra can be deconvoluted into four sub-peaks, consisting of C–C at ~ 284.7 eV, C=N at ~ 285.1 eV, C–O at 286.2 eV, and C=C at 289.8 eV (Fig. S22 in the ESM) [41]. In the normalized Raman spectra, Co/Co-N-C/CC with an I_D/I_G value of 1.35 (Fig. 4(i)), reflects a large number of defects in the partial graphitization of carbon. Furthermore, the N 1s XPS spectra in Fig. 4(j) indicates the coexistence of active Co–N_x bonding (~ 398.9 eV) and graphitic N (~ 401.3 eV) [42, 43].

To identify the important role of the unsaturated coordinated ZIFs in facilitating the ZIFs growth on carbon cloth, the cathode properties of Co/Co-N-C/CC as air electrode in rechargeable Zn-air battery were tested. Figure 5(a) displays the scheme of homemade liquid-state ZAB test system. After weighing the ZIF-S@CC before and after carbonization, the average catalyst loading was calculated to be around 0.2 mg·cm^{-2}. As expected, the liquid-state ZABs with Co/Co-N-C/CC cathode exhibits much-enhanced cycling stability after continuous 70 h operation for 630 cycles with a high energy efficiency of 61% (Fig. 5(b)). The

voltage efficiency and the galvanodynamic behavior of Co/Co-N-C/CC cathode are comparable to that of benchmarking Pt/C-IrO$_2$ mixture (mass ratio 1:1, unit loading 1 mg·cm^{-2}) as verified in Figs. 5(c) and 5(d). Notably, the peak power density of the ZAB using the Co/Co-N-C/CC anode is high up to 163 mW·cm^{-2} at 129 mA·cm^{-2}, and is 40 mW·cm^{-2} higher than that of Pt/C-IrO$_2$ catalysts (Fig. 5(e)), which is also comparable to the best electrocatalysts [44]. The specific capacity was calculated and normalized by Zn mass. Even at 50 mA·cm^{-2}, the liquid-state ZAB with Co/Co-N-C/CC cathode delivers an ultra-high specific capacity of 833 mAh·g^{-1} and a large energy density of 983 Wh·kg^{-1}, which is approximately 91% of the theory values of ZAB and 1.5-fold larger than that of Pt/C benchmark (653 mAh·g^{-1}) (see Fig. 5(f)). To demonstrate the usability of our cathode in the flexible and solid-state ZAB, it is directly used as the cathode for the assembling of solid-state ZAB (Fig. 5(g)). One blue light-emitting diode (LED) (5 mm, 3.2 V) is lighted by three flexible solid-state ZABs in series. The Co/Co-N-C/CC assembled flexible solid-state ZAB exhibits an open-circuit voltage of 1.439 V (Fig. 5(h)), which is much higher than that of commercial Pt/C-IrO$_2$ (mass ratio 1:1) (1.395 V). Such result is also superior to those in the recent reports (see Table S4 in the ESM). This fully shows the feasibility of our Co/Co-N-C/CC cathode to enhance operation effectiveness and long-term charge–discharge of existing practical ZABs.

3 Conclusions

In summary, we have designed a robust self-supported air electrode consisting of Co NPs uniformly confined within Co-N-C matrix on the acid-treated carbon cloth (Co/Co-N-C/CC). Although ZIF powders without carbon cloth present a slight difference in bifunctional oxygen electrolysis. By rationally tuning
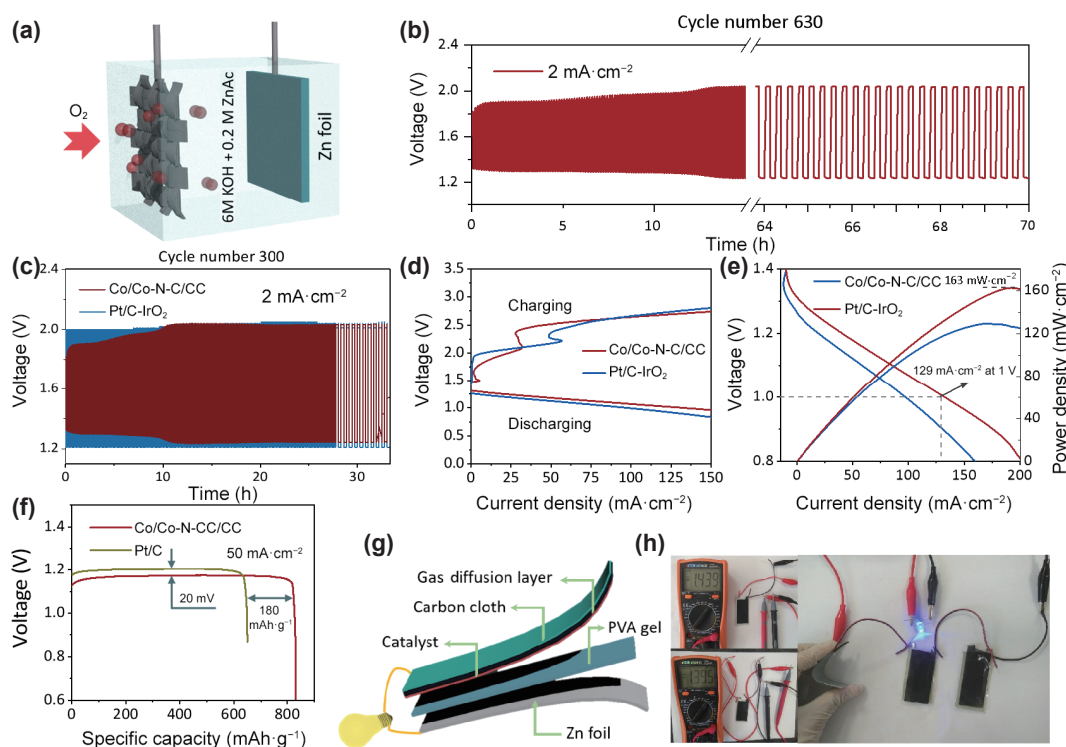

Figure 5 Fabrication and performance of rechargeable ZAB. (a) Schematic diagram of the structure of the assembled ZAB. (b) Galvanostatic discharge–charge cycling curve at 2 mA·cm^{-2} of two-electrode rechargeable ZAB with the Co/Co-N-C/CC air electrode; (c) cycling performance of the ZAB with Co/Co-N-C/CC (red line) and Pt/C-IrO$_2$ (blue line, loading 1 mg·cm^{-2}) cathodes at a current density of 2 mA·cm^{-2}. (d) Galvanodynamic charge–discharge polarization curves of two-electrode ZAB using Co/Co-N-C/CC as air electrodes, together with the corresponding curve (Pt/C-IrO$_2$); (e) polarization and power density curves of primary ZABs using Pt/C-IrO$_2$ and Co/Co-N-C/CC as ORR catalyst (mass loading of 1 mg·cm^{-2}) at a scan rate of 5 mV·s^{-1}; and (f) specific discharging capacities at 50 mA·cm^{-2} of Pt/C and Co/Co-N-CC/CC. (g) Schematic of wearable all-solid-state ZAB. (h) Photograph of a lighted blue LED (5 mm, ~ 3.2 V) powered by three all-solid-state ZABs interconnected in series, photograph of the assembled all-solid-state ZAB using Co/Co-N-C/CC as air electrodes exhibiting open circuit voltage of ~ 1.439 V measured with a voltmeter, photograph of the assembled all-solid-state ZAB using Pt/C-IrO$_2$ as air electrodes exhibiting a minimum open circuit voltage of ~ 1.395 V measured with a voltammeter.

the unsaturated coordination levels of morphology-induced ZIFs, high unsaturated coordination ZIF is tightly combined with carbon cloth. The as-synthesized Co/Co-N-C/CC constructs a strong air cathode with a larger open-circuit voltage, immenser power density, and superior durability upon 630 cycles, significantly surpassing the benchmark Pt/C-IrO₂. The superior electrocatalytic activities of the catalyst are ascribed to the high-density of open active sites, excellent conductivity, and strong catalyst-support combination as well as the synergy of Co NPs and local active Co-N-C centers. Our study not only provides an effective strategy for the design and assemble of high-performance, non-noble-metal-based bifunctional oxygen electrocatalysts for ZABs, but also gives a deep understanding about the relationship betweeen the open coordination structures of ZIF precursors and electrochemical properties of their derivatives.

Acknowledgement

Electronic Supplementary Material: Supplementary material (additional material characterization such as SEM images, TEM images, HRTEM images, XRD patterns, Raman spectra, ICP, XPS results, and electrochemical test results) is available in the online version of this article at https://doi.org/10.1007/s12274-022-4243-4.

References

[1] Lee, J. S.; Kim, S. T.; Cao, R. G.; Choi, N. S.; Liu, M. L.; Lee, K. T.; Cho, J. Metal-air batteries with high energy density: Li-air versus Zn-air. *Adv. Energy Mater.* **2011**, *1*, 34–50.

[2] Meng, F. L.; Liu, K. H.; Zhang, Y.; Shi, M. M.; Zhang, X. B.; Yan, J. M.; Jiang, Q. Recent advances toward the rational design of efficient bifunctional air electrodes for rechargeable Zn-air batteries. *Small* **2018**, *14*, 1703843.

[3] Li, J. K.; Alsudairi, A.; Ma, Z. F.; Mukerjee, S.; Jia, Q. Y. Asymmetric volcano trend in oxygen reduction activity of Pt and non-Pt catalysts: *In situ* identification of the site-blocking effect. *J. Am. Chem. Soc.* **2017**, *139*, 1384–1387.

[4] Li, W. D.; Zhao, Y. X.; Liu, Y.; Sun, M. Z.; Waterhouse, G. I. N.; Huang, B. L.; Zhang, K.; Zhang, T. R.; Lu, S. Y. Exploiting Ru-induced lattice strain in CoRu nanoalloys for robust bifunctional hydrogen production. *Angew. Chem., Int. Ed.* **2021**, *60*, 3290–3298.

[5] Song, H. Q.; Wu, M.; Tang, Z. Y.; Tse, J. S.; Yang, B.; Lu, S. Y. Single atom ruthenium-doped CoP/CDs nanosheets via splicing of carbon-dots for robust hydrogen production. *Angew. Chem., Int. Ed.* **2021**, *60*, 7234–7244.

[6] Han, A. L.; Wang, X. J.; Tang, K.; Zhang, Z. D.; Ye, C. L.; Kong, K. J.; Hu, H. B.; Zheng, L. R.; Jiang, P.; Zhao, C. X. et al. An adjacent atomic platinum site enables single-atom iron with high oxygen reduction reaction performance. *Angew. Chem., Int. Ed.* **2021**, *60*, 19262–19271.

[7] Li, X. Y.; Rong, H. P.; Zhang, J. T.; Wang, D. S.; Li, Y. D. Modulating the local coordination environment of single-atom catalysts for enhanced catalytic performance. *Nano Res.* **2020**, *13*, 1842–1855.

[8] Wang, Y.; Zheng, X. B; Wang, D. S. Design concept for electrocatalysts. *Nano Res.* **2022**, *15*, 1730–1752.

[9] Song, H. Q.; Li, Y. H.; Shang, L.; Tang, Z. Y.; Zhang, T. R.; Lu, S. Y. Designed controllable nitrogen-doped carbon-dots-loaded MoP nanoparticles for boosting hydrogen evolution reaction in alkaline medium. *Nano Energy* **2020**, *72*, 104730.

[10] Cui, T. T.; Wang, Y. P.; Ye, Y.; Wu, J.; Chen, Z. Q.; Li, J.; Lei, Y. P.; Wang, D. S.; Li, Y. D. Engineering dual single-atom sites on 2D ultrathin N-doped carbon nanosheets attaining ultra-low-temperature zinc-air battery. *Angew. Chem., Int. Ed.* **2022**, *61*, e202115219.

[11] Zhang, L.; Zhu, J. W.; Li, X.; Mu, S. C.; Verpoort, F.; Xue, J. M.; Kou, Z. K.; Wang, J. Nurturing the marriages of single atoms with atomic clusters and nanoparticles for better heterogeneous electrocatalysis. *Interdiscip. Mater.* **2022**, *1*, 51–87.

[12] Wu, W. J.; Liu, Y.; Liu, D.; Chen, W. X.; Song, Z. Y.; Wang, X. M.; Zheng, Y. M.; Lu, N.; Wang, C. X.; Mao, J. J. et al. Single copper sites dispersed on hierarchically porous carbon for improving oxygen reduction reaction towards zinc-air battery. *Nano Res.* **2021**, *14*, 998–1003.

[13] Hu, B. T.; Huang, A. J.; Zhang, X. J.; Chen, Z.; Tu, R. Y.; Zhu, W.; Zhuang, Z. B.; Chen, C.; Peng, Q.; Li, Y. D. Atomic Co/Ni dual sites with N/P-coordination as bifunctional oxygen electrocatalyst for rechargeable zinc-air batteries. *Nano Res.* **2021**, *14*, 3482–3488.

[14] Zhang, Z. W.; Jin, H. H.; Zhu, J. W.; Li, W. Q.; Zhang, C. T.; Zhao, J. H.; Luo, F.; Sun, Z. G.; Mu, S. C. 3D flower-like ZnFe-ZIF derived hierarchical Fe, N-Codoped carbon architecture for enhanced oxygen reduction in both alkaline and acidic media, and zinc-air battery performance. *Carbon* **2020**, *161*, 502–509.

[15] Amiinu, I. S.; Liu, X. B; Pu, Z. H; Li, W. Q; Li, Q. D; Zhang, J.; Tang, H. L.; Zhang, H. N.; Mu, S. C. From 3D ZIF nanocrystals to Co-Nₓ/C nanorod array electrocatalysts for ORR, OER, and Zn-air batteries. *Adv. Funct. Mater.* **2018**, *28*, 1704638.

[16] Tana, P.; Chen, B.; Xua, H. R.; Zhang, H. C.; Cai, W. Z.; Ni, M.; Liu, M. L.; Shao, Z. P. Flexible Zn- and Li-air batteries: Recent advances, challenges, and future perspectives. *Energy Environ. Sci.* **2017**, *10*, 2056–2080.

[17] Jiang, Y.; Deng, Y. P.; Liang, R. L.; Fu, J.; Gao, R.; Luo, D.; Bai, Z. Y.; Hu, Y. F.; Yu, A. P.; Chen, Z. W. d-Orbital steered active sites through ligand editing on heterometal imidazole frameworks for rechargeable zinc-air battery. *Nat. Commun.* **2020**, *11*, 5858.

[18] Yan, X. X.; Ha, Y.; Wu, R. B. Binder-free air electrodes for rechargeable zinc-air batteries: Recent progress and future perspectives. *Small Methods* **2021**, *5*, 2000827.

[19] Zang, W. J.; Sumboja, A.; Ma, Y. Y.; Zhang, H.; Wu, Y.; Wu, S. S.; Wu, H. J.; Liu, Z. L.; Guan, C.; Wang, J. et al. Single Co atoms anchored in porous N-doped carbon for efficient zinc-air battery cathodes. *ACS Catal.* **2018**, *8*, 8961–8969.

[20] Guan, C.; Sumboja, A.; Wu, H. J.; Ren, W. N.; Liu, X. M.; Zhang, H.; Liu, Z. L.; Cheng, C. W.; Pennycook, S. J.; Wang, J. Hollow Co₃O₄ nanosphere embedded in carbon arrays for stable and flexible solid-state zinc-air batteries. *Adv. Mater.* **2017**, *29*, 1704117.

[21] Xie, J. P.; Li, J. L.; Li, X. D.; Lei, H.; Zhuo, W. C.; Li, X. B.; Hong, G.; Hui, K. N.; Pan, L. K.; Mai, W. J. Ultrahigh "relative energy density" and mass loading of carbon cloth anodes for K-ion batteries. *CCS Chem.* **2020**, *3*, 791–799.

[22] Zhu, L.; Zheng, D. Z.; Wang, Z. F.; Zheng, X. S.; Fang, P. P.; Zhu, J. F.; Yu, M. H.; Tong, Y. X.; Lu, X. H. A confinement strategy for stabilizing ZIF-derived bifunctional catalysts as a benchmark cathode of flexible all-solid-state zinc-air batteries. *Adv. Mater.* **2018**, *30*, 1805268.

[23] Li, X.; Li, Z. H.; Lu, L.; Huang, L. M.; Xiang, L.; Shen, J.; Liu, S. Y.; Xiao, D. R. The solvent induced inter-dimensional phase transformations of cobalt zeolitic-imidazolate frameworks. *Chem. —Eur. J.* **2017**, *23*, 10638–10643.

[24] Chen, R. Z.; Yao, J. F.; Gu, Q. F.; Smeets, S.; Baerlocher, C.; Gu, H. X.; Zhu, D. R.; Morris, W.; Yaghi, O. M.; Wang, H. T. Two-dimensional zeolitic imidazolate framework with a cushion-shaped cavity for CO₂ adsorption. *Chem. Commun.* **2013**, *49*, 9500–9502.

[25] Low, Z. X.; Yao, J. F.; Liu, Q.; He, M.; Wang, Z. Y.; Suresh, A. K.; Bellare, J.; Wang, H. T. Crystal transformation in zeolitic-imidazolate framework. *Cryst. Growth Des.* **2014**, *14*, 6589–6598.

[26] Yang, F.; Xie, J. H.; Liu, X. Q.; Wang, G. Z.; Lu, X. H. Linker defects triggering boosted oxygen reduction activity of Co/Zn-ZIF nanosheet arrays for rechargeable Zn-air batteries. *Small* **2021**, *17*, 2007085.

[27] Zhou, K.; Mousavi, B.; Luo, Z. X.; Phatanasri, S.; Chaemchuen, S.; Verpoort, F. Characterization and properties of Zn/Co zeolitic imidazolate frameworks vs. ZIF-8 and ZIF-67. *J. Mater. Chem. A* **2017**, *5*, 952–957.

[28] Kim, D. W.; Kang, D. W.; Kang, M.; Lee, J. H.; Choe, J. H.; Chae,

Y. S.; Choi, D. S.; Yun, H.; Hong, C. S. High ammonia uptake of a metal-organic framework adsorbent in a wide pressure range. *Angew. Chem.* **2020**, *132*, 22720–22725.

[29] Yi, F. Y.; Zhang, R.; Wang, H. L.; Chen, L. F.; Han, L.; Jiang, H. L.; Xu, Q. Metal-organic frameworks and their composites: Synthesis and electrochemical applications. *Small Methods* **2017**, *1*, 1700187.

[30] Chen, Z. L.; Ha, Y.; Jia, H. X.; Yan, X. X.; Chen, M.; Liu, M.; Wu, R. B. Oriented transformation of Co-LDH into 2D/3D ZIF-67 to achieve Co-N-C hybrids for efficient overall water splitting. *Adv. Energy Mater.* **2019**, *9*, 1803918.

[31] Chen, Y. S.; Zhang, W. H.; Zhu, Z. Y.; Zhang, L. L.; Yang, J. Y.; Chen, H. H.; Zheng, B.; Li, S; Zhang, W. N.; Wu, J. S. et al. Co nanoparticles combined with nitrogen-doped graphitic carbon anchored on carbon fibers as a self-standing air electrode for flexible zinc-air batteries. *J. Mater. Chem. A* **2020**, *8*, 7184–7191.

[32] Shen, M. X.; Zheng, L. R.; He, W. H.; Ruan, C. P.; Jiang, C. H.; Ai, K. J.; Lu, L. H. High-performance oxygen reduction electrocatalysts derived from uniform cobalt-adenine assemblies. *Nano Energy* **2015**, *17*, 120–130.

[33] Ahn, S. H.; Manthiram, A. Cobalt phosphide coupled with heteroatom-doped nanocarbon hybrid electroctalysts for efficient, long-life rechargeable zinc-air batteries. *Small* **2017**, *13*, 1702068.

[34] Yan, L. T.; Xu, Y. L.; Chen, P.; Zhang, S.; Jiang, H. M.; Yang, L. Z.; Wang, Y.; Zhang, L.; Shen, J. X.; Zhao, X. B. et al. A freestanding 3D heterostructure film stitched by MOF-derived carbon nanotube microsphere superstructure and reduced graphene oxide sheets: A superior multifunctional electrode for overall water splitting and Zn-air batteries. *Adv. Mater.* **2020**, *32*, 2003313.

[35] Wang, Y. Y.; Kumar, A.; Ma, M.; Jia, Y.; Wang, Y.; Zhang, Y.; Zhang, G. X.; Sun, X. M.; Yan, Z. F. Hierarchical peony-like FeCo-NC with conductive network and highly active sites as efficient electrocatalyst for rechargeable Zn-air battery. *Nano Res.* **2020**, *13*, 1090–1099.

[36] Jiang, G. Y.; Jiang, N.; Zheng, N.; Chen, X.; Mao, J. Y.; Ding, G. Y.; Li, Y. H.; Sun, F. G.; Li, Y. S. MOF-derived porous Co3O4-NC nanoflake arrays on carbon fiber cloth as stable hosts for dendrite-free Li metal anodes. *Energy Storage Mater.* **2019**, *23*, 181–189.

[37] Wang, R. R.; Wu, R. B.; Yan, X. X.; Liu, D.; Guo, P. F.; Li, W.; Pan, H. G. Implanting single Zn atoms coupled with metallic Co nanoparticles into porous carbon nanosheets grafted with carbon nanotubes for high-performance lithium-sulfur batteries. *Adv. Funct. Mater.*, in press, https://doi.org/ 10.1002/adfm.202200424.

[38] Jiang, Y.; Deng, Y. P.; Liang, R. L.; Fu, J.; Luo, D.; Liu, G. H.; Li, J. D.; Zhang, Z.; Hu, Y. F.; Chen, Z. W. Multidimensional ordered bifunctional air electrode enables flash reactants shuttling for high-energy flexible Zn-air batteries. *Adv. Energy Mater.* **2019**, *9*, 1900911.

[39] Wang, T. T.; Kou, Z. K.; Mu, S. C.; Liu, J. P.; He, D. P.; Amiinu, I. S.; Meng, W.; Zhou, K.; Luo, Z. X.; Chaemchuen, S. et al. 2D dual-metal zeolitic-imidazolate-framework-(ZIF)-derived bifunctional air electrodes with ultrahigh electrochemical properties for rechargeable zinc-air batteries. *Adv. Funct. Mater.* **2018**, *28*, 1705048.

[40] You, B.; Jiang, N.; Sheng, M. L.; Drisdell, W. S.; Yano, J.; Sun, Y. J. Bimetal-organic framework self-adjusted synthesis of support-free nonprecious electrocatalysts for efficient oxygen reduction. *ACS Catal.* **2015**, *5*, 7068–7076.

[41] Ren, D. Z.; Ying, J.; Xiao, M. L.; Deng, Y. P.; Ou, J. H.; Zhu, J. B.; Liu, G. H.; Pei, Y.; Li, S.; Jauhar, A. M. et al. Hierarchically porous multimetal-based carbon nanorod hybrid as an efficient oxygen catalyst for rechargeable zinc-air batteries. *Adv. Funct. Mater.* **2020**, *30*, 1908167.

[42] Ahn, S. H.; Klein, M. J.; Manthiram, A. 1D Co- and N-doped hierarchically porous carbon nanotubes derived from bimetallic metal organic framework for efficient oxygen and tri-iodide reduction reactions. *Adv. Energy Mater.* **2017**, *7*, 1601979.

[43] Guo, D. H.; Shibuya, R.; Akiba, C.; Saji, S.; Kondo, T.; Nakamura, J. Active sites of nitrogen-doped carbon materials for oxygen reduction reaction clarified using model catalysts. *Science* **2016**, *351*, 361–365.

[44] Yan, L. T.; Xu, Y. L.; Chen, P.; Zhang, S.; Jiang, H. M.; Yang, L. Z.; Wang, Y.; Zhang, L.; Shen, J. X.; Zhao, X. B. et al. A freestanding 3D heterostructure film stitched by MOF-derived carbon nanotube microsphere superstructure and reduced graphene oxide sheets: A superior multifunctional electrode for overall water splitting and Zn-air batteries. *Adv. Mater.* **2020**, *32*, 2003313.